PAPER

Check for updates

Organic template-based ZnO embedded Mn$_3$O$_4$ nanoparticles: synthesis and evaluation of their electrochemical properties towards clean energy generation†

Taghazal Zahra,[a] Khuram Shahzad Ahmad, [ID] *[a] Andrew Guy Thomas, [ID] [c] Camila Zequine,[b] Mohammad Azad Malik[c] and Ram K. Gupta[b]

To deal with fossil fuel depletion and the rise in global temperatures caused by fossil fuels, cheap and abundant materials are required, in order to fulfill energy demand by developing high-performance fuel cells and electrocatalysts. In this work, a natural organic agent has been used to synthesize nano-structured ZnO/Mn$_3$O$_4$ with high surface area and enhanced electrocatalytic performance. Upon pre-annealing treatment, mixed metal oxide precipitates are formed due to the complex formation between a metal oxide and organic extract. The thermally annealed mixed oxide ZnO/Mn$_3$O$_4$ was characterized by XRD diffractometer, Fourier transform infrared spectroscopy (FTIR), X-ray photoelectron spectroscopy (XPS), field emission scanning electron microscopy (FE-SEM), transmission electron microscopy (TEM) and energy dispersive X-ray spectroscopy (EDX). Gas chromatography-mass spectrometry (GC-MS) identified methyldecylamine as a major stabilizing agent of the synthesized nanomaterial. Using a Tauc plot, the calculated band energy for the synthesized ZnO/Mn$_3$O$_4$ mixed metal oxide was 1.65 eV. Moreover, we have demonstrated the effects of incorporated organic compounds on the surface chemistry, morphology and electrochemical behavior of ZnO/Mn$_3$O$_4$. The phyto-functionalized ZnO/ Mn$_3$O$_4$ was deposited on Ni-foam for electrocatalytic studies. The fabricated electrode revealed good performance with low over-potential and Tafel slope, suggesting it to be suitable as a potential catalyst for water splitting application, in particular for the oxygen evolution reaction (OER). The overall findings of the current study provide a cost-effective and efficient organic template for functionalization and sustainable fabrication of ZnO/Mn$_3$O$_4$ nanomaterial for application as an electrocatalyst.

1. Introduction

Increasing energy demand, the greenhouse effect, and rapid depletion of fossil fuels have motivated researchers towards the development of products designed for the generation of alternative, clean and sustainable energy.[1–113] In order to fulfill energy demands, electrochemical water splitting is one of the eco-friendly and alternative pathways for energy generation.[2,3] The water splitting mechanism is the reverse of the fuel cell reaction and comprises anodic, oxygen evolution reaction (OER) and the cathodic, hydrogen evolution reaction (HER). The

hydrogen evolution reaction on the cathode not only favors a viable route to produce hydrogen from water but is also an important component in the development of fuel cell devices.[4] However, due to sluggish kinetics and a large anodic over-potential in the oxygen evolution reaction (OER), water oxidation is hampered in an alkaline medium.[5–10] To deal with this, significant efforts have been made to design an efficient electrode material which performs best in alkaline medium with a low OER/HER over-potential.[7–12]

Currently, noble metals such as ruthenium oxide (RuO$_2$), iridium oxide (IrO$_2$), and Pt-based materials are considered as benchmark HER and OER catalysts because of their efficient electro-hindered due to the high cost and low earth abundance. Therefore, it is desirable to explore such bi-functional electrode materials that have low cost, high abundance and high electro-catalytic efficiency with large scale applicability towards OER and HER. Zinc oxide is an interesting transition metal oxide due to its chemical stability, abundance and wide applications in optical and electronic devices making it the best fit for wide application,[13] but its poor electric conductivity

[a]*Department of Environmental Sciences, Fatima Jinnah Women University, Rawalpindi, Pakistan. E-mail: chemist.phd33@yahoo.com; dr.k.s.ahmad@fjwu.edu. pk*

[b]*Department of Chemistry, Pittsburg State University, 1701 South Broadway Street, Pittsburg, KS 66762, USA*

[c]*Department of Materials, Photon Science Institute, Sir Henry Royce Institute, Alan Turing Building, The University of Manchester, Oxford Road, Manchester M13 9PL, UK*

and high resistance limits its use as electrode material.[14–16] To overcome this problem, a principle approach is to tailor the morphology in order to enhance the surface area of ZnO. It is well known that high surface area improves the charge-transfer capability and enriches the interaction of electrolyte with the electrode surface thus enhancing the diffusion of ions.[17–21] In addition, an alternative to reduce the drawbacks associated with ZnO is to combine it with other metals or metal oxides.[22,23] Doping of different metallic ions and formation of binary mixed metals/metal oxides improves the electric, magnetic, electrochromic and catalytic properties of ZnO.[24–27,106] For the resolution of the challenges associated with ZnO utilization, manganese and manganese-based catalysts are gaining thrust for application in catalytic and fuel cell devices. This is due to their low cost and improved activity compared to Pt-based rare earth metals.[28–32] Therefore, combining Mn oxide with cheap and abundant ZnO is an effective way to improve the electro catalytic activity due to the diversifying the properties of the combination of different components.[33] Previously, binary/mixed metals/metal oxides have been prepared by different physical and the chemical synthesis routes. However, the chemical and physical synthesis method involves chemical reagents or stabilizing agents that are a major concern towards environmental safety and sustainability.[34–36] In this context, successive phyto-synthetic routes have been investigated and reported,[37,38,42–46] and have many advantages in terms of reduced toxicity, and the simplicity of method over the chemical synthesis approach.[39,40,83] In the present study, bio-templated mixed metal oxides have been investigated as a facile, greener nano-material with enhanced surface properties to replace chemically synthesized material. Thus, the focus of the present study is the synthesis of ZnO/Mn$_3$O$_4$ nano-material using leaf extracts of the *Olea ferruginea* Royle (OFR) plant taken from Azad Jammu Kashmir, Pakistan. The selected plant is known for its richness in biologically active compounds *i.e.* phenols, flavonoids and alkaloids.[84,85] Secondly, the plant has not been explored before as a bio reductant in the synthesis of mixed metal oxides. We have tuned the surface morphology of ZnO/Mn$_3$O$_4$ by incorporating carbon and oxygen species as the bioactive compounds aided by the OFR organic extract. Previously, the surface of functionalized nanomaterials has been improved by incorporating carbon, oxygen nitrogen-containing groups using synthetic reagents which enhance the electrochemical performance of catalyst for fuel cell application.[63,86–88] Similarly, related carbon structures including carbon,[89] graphene,[90] carbon fibers[92] and carbon nanotubes[91] have been reported as practicable materials with excellent performance in OER. N-doped carbon materials have been studied extensively for electrochemical studies.[93] The present synthesis approach offers a green synthesis route without the involvement of any auxiliary chemical reagents for the synthesis of ZnO/Mn$_3$O$_4$ nanoparticles. Thus, we believe that the proposed bio template-assisted synthesis route can significantly affect the efficiency of the ZnO/Mn$_3$O$_4$ nano catalyst towards renewable energy to facilitate fast diffusion of ions and current charge carriers.

2. Experimental details

Olea ferruginea Royle (OFRL) sampling and extract preparation were done by following orthodox protocols.[94–97] Using the organic extract as a reducing and stabilizing agent, ZnO/Mn$_3$O$_4$ nanoparticles (NPs) were synthesized by simply modifying the co-precipitation method (Fig. 1) in which chemical reagents have been used previously.[42–46,98–100] 20 mM salt solution was prepared by mixing zinc(II) acetate dihydrate: Zn(CH$_3$COO)$_2$·2H$_2$O and manganese(II) acetate tetrahydrate: Mn(CH$_3$CO$_2$)$_2$·4H$_2$O separately in 250 ml of distilled water with continuous stirring at room temperature for 20 min. These solutions were combined together with 10 ml of organic extract and the mixture were stirred continuously at 80 °C for an hour. An immediate color change and precipitates formation was observed indicating the initiation of nanoparticles formation. The organic extract aids in the reduction of metal salts to zero-valent metals as presented in Fig. 1. After heating and stirring, the solution was left overnight for incubation at room temperature and then centrifuged at 6000 rpm for 20 minutes. The incorporated organic content results in the stabilization of formed particles leading to the production of dark brown precipitates. Before oven drying at 95 °C, the as-prepared ZnO/Mn$_3$O$_4$ product was washed several times with double-distilled water and then with ethanol. The dried powder was ground to a fine powder and placed in a muffle furnace (D550, Ney Vulcan, USA) at 450 °C to produce ZnO/Mn$_3$O$_4$ NPs.

Phytochemical analysis of the extract and synthesized mixed metal oxide nanoparticles (ZnO/Mn$_3$O$_4$ NPs) were characterized by UV-vis spectroscopy (1602, Biomedical services, Spain) FTIR; Fourier transform infrared spectroscopy (8400, Shimadzu, Japan) and gas chromatography-mass spectroscopy (GC-MS) to identify the organic compounds acting as stabilizing or capping agents. The crystalline phase of the ZnO/Mn$_3$O$_4$ was examined by XRD diffractometer (Bruker Advanced X-ray Solutions D9). X-ray photoelectron spectroscopy (XPS) spectra were collected using a Kratos Axis Ultra Spectrometer (Monochromated Al Kα X-ray source, $h\nu$ = 1486.6 eV) to determine surface chemistry. Energy dispersive X-ray spectroscopy (EDX) was used to confirm the purity and the bulk elemental composition of the synthesized material. Structure and morphology were observed by using Quanta-250 FEG scanning electron microscopy (FE-SEM) and FEI Titan G2 80-200 scanning transmission electron microscope (TEM).

Fabrication of a working electrode (ZnO/Mn$_3$O$_4$) was done by mixing 80 wt% of the synthesized NPs, 10 wt% of acetylene black, and 10 wt% of polyvinylidene difluoride (PVDF) in the presence of *N*-methyl pyrrolidinone (NMP). After homogeneous mixing, the slurry was deposited on Ni-foam and dried at 60 °C under vacuum for 12 hours. Nickel foam (1.5 mm; 1 × 2 cm) was used as the mechanical support to the electro-catalyst (ZnO/Mn$_3$O$_4$). The mass loading of electrocatalyst was 2 mg cm^{-2}.

The catalytic activity of synthesized material was studied using a VersaSTAT 4-500 electrochemical workstation (Princeton Applied Research, USA) in standard electrode configuration with 1 M KOH electrolyte solution. A graphite rod, saturated
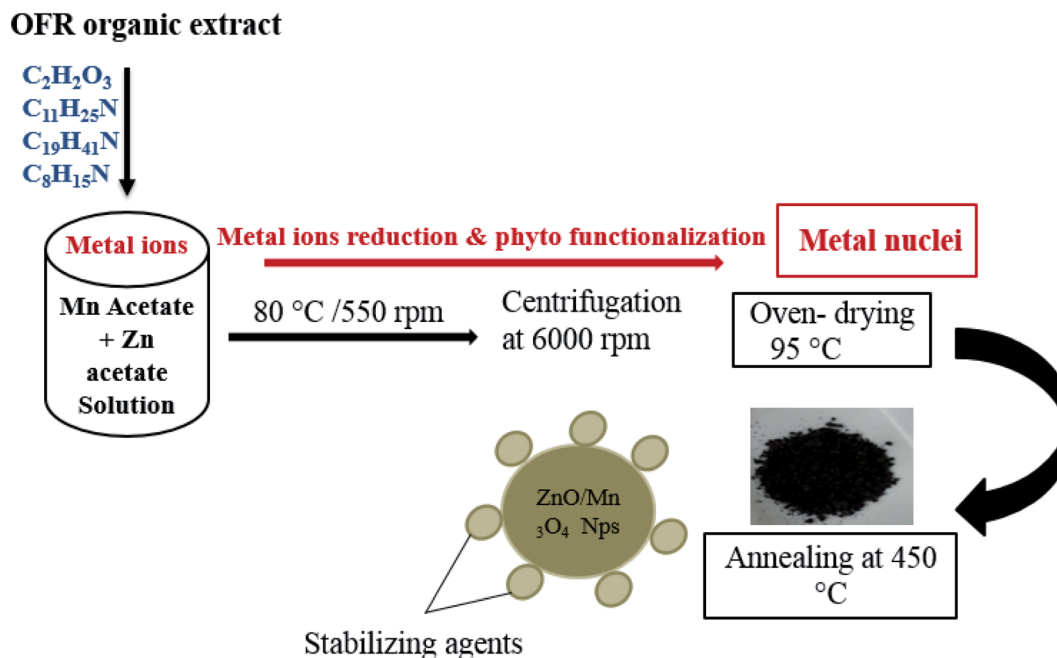
OFR organic extract

Fig. 1 Schematic diagram of the synthesis procedure and mechanism of phyto-functionalized ZnO/Mn$_3$O$_4$ NPs.

calomel electrode (SCE), and synthesized ZnO/Mn$_2$O$_3$@Ni-foam were used as a counter, reference and working electrode, respectively. Electro-catalytic testing including linear sweep voltammetry (LSV) and electrochemical impedance spectroscopy (EIS) were performed. LSV was performed at a rate of 1 mV s^{-1} for both OER and HER. Using the Nernst equation the potential was converted to RHE (eqn (1)).[41] All EIS measurements were conducted in an applied AC amplitude of 10 mV with the frequency range of 0.05 Hz to 10 kHz.

$$E(RHE) = E(Ag/AgCl) + (0.205 + 0.059 \times pH) \qquad (1)$$

3. Result and discussion

The phytochemical analysis and all the relevant detail are given in Fig. S-1, Tables S-1 and S-2.† UV-visible spectroscopy shows absorbance at 271, 327 and 400 nm. The prominent peaks were noticed in the ultra violet and the visible region as shown in the Fig. S-1.† These peaks corresponds to plant phenols, flavonoids and flavonols. The dried powder of the OFR leaf was subjected to FTIR over the range of 400–4000 cm^{-1} to determine the chemistry of phyto compounds of the selected plant. Table S-2† summarizes the vibrational frequencies of specific functional groups assigned the aliphatic amines and alkenes present in the leaf powder. The frequency range from 3400–2922 cm^{-1} represents the O–H stretching vibration and –C=C– stretch suggesting the presence of alcohols and phenols; alkanes and alkenes, respectively. The frequencies (cm^{-1}) 1600 and 1100 suggested the presence of nitro compounds; aromatic amines; alcohols, carboxylic acids, esters and ethers. At frequencies 1030 cm^{-1} and 875 cm^{-1}, C–N stretch and =C–H bend

attributed to aliphatic amines and alkenes are observed. A weak vibrational mode at 798.56 cm^{-1} has been noticed and is assigned to a =C–H bend and C–Cl stretch. GC-MS analysis of the methanolic extract of OFR plant extract identified various compounds as follows. The major bioactive compounds identified in OFR were benzenemethanol, cathinone, 3-azabicyclo nonane, propanedioic acid, 1-cyclohexylethylamine. In agreement with FTIR results, GCMS illustrates majority of the NH-bond containing compounds are amino acids and amines with the highest weight % of cathinone. Cathinone is a monoamine alkaloid having a ketone group. After cathinone, the highest weight % is of 1-cyclohexylethylamine, benzenemethanol and propanedioic acid. The structures of 1-cyclohexylethylamine, benzenemethanol and propanedioic acid are given in Table S-3† indicate the presence of phenols, flavonoids and amine groups as proposed by spectroscopic analysis.

FTIR of the synthesized nano-powder is carried out to confirm the role of organic content of OFR in the synthesis of NPs. The FTIR spectrum is shown in Fig. 2a that shows vibrational peaks at 2580 cm^{-1} (O–H$_{str}$, carboxylic acid), 1104 cm^{-1} (CO$_{str}$, alcohols, carboxylic acids, esters, ether) and 958 cm^{-1} (C–N$_{str}$, aromatic amines), =C–H bend suggesting alkenes. The inset in Fig. 2a covering 400–600 cm^{-1} shows peaks at 412 cm^{-1}, 421 cm^{-1}, 437 cm^{-1}, 491 cm^{-1} and 517 cm^{-1} corresponding to M–C and M–O (where M = metal ion) bonds suggesting metal oxides of manganese and zinc.

In agreement with the composition of plant extract, GC-MS analysis of ZnO/Mn$_3$O$_4$ confirmed the role of OFR extract as a capping agent in the synthesis. In Fig. 2b the GC-MS chromatogram exhibits a sharp peak at 20.90 retention time corresponding to methyldecylamine (amine derivative) which is an antioxidant present in medicinal plants.[47] It is proposed in the
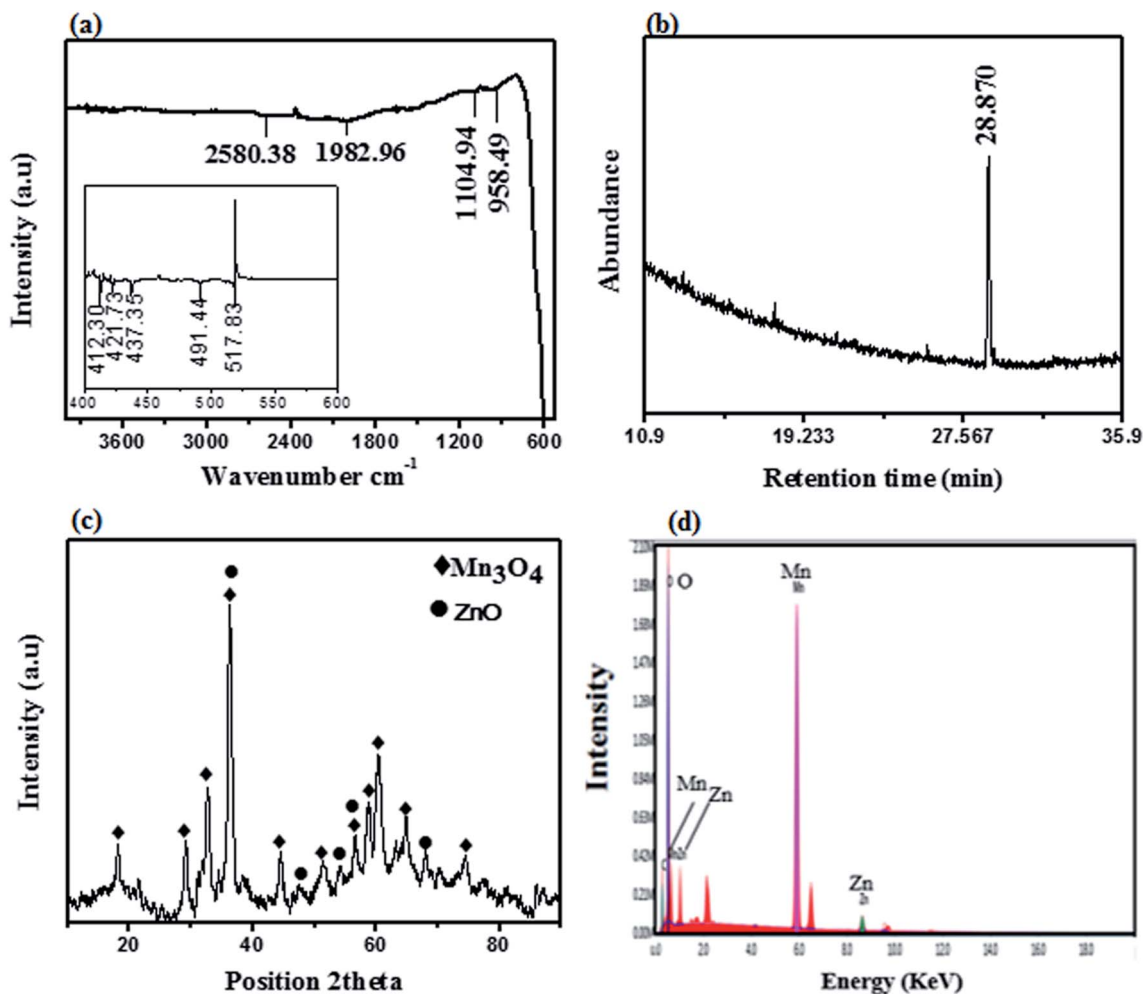
Fig. 2   (a) FTIR spectrum (b) GC–MS chromatogram (c) X-ray diffractogram and (d) EDX spectra of as synthesized ZnO/Mn_3O_4 NPs.

light of previous studies[63,86,89] that these organic compounds could improve the electrochemical performance of synthesized material by enhancing the electron flow.

The purity and crystallinity of as-synthesized material were examined by powder X-ray diffraction (p-XRD). The XRD pattern of ZnO/Mn_3O_4 mixed metal oxide is shown in Fig. 2c. The relative peak intensities and position of Mn_3O_4 and ZnO diffraction peaks are in good agreement with JCPDS card no. 00-024-0734 and 00-036-1451, respectively. Mn_3O_4 exhibits a tetragonal hausmannite crystal system with cell parameters, $a = 5.7$, $b = 5.7$, $c = 9.4$ Å. Prominent diffraction peaks indicated by ($\blacklozenge$) at 2θ values of $18°$, $32.36°$ and $36.986°$, $44.44°$, $58.5°$ and $60.634°$ are associated with (101), (103), (211), (220), (321) and (215) planes respectively in good agreement with literature values. ZnO exhibits a hexagonal crystal system with cell parameters of $a = 3.2$, $b = 3.2$, $c = 5.2$ Å and introduce distinctive characteristic peaks denoted by (*) at $2\theta = 36.253°$, $56.60°$ and $67.96°$ due to reflection of (101), (110) and (112), Miller index planes, respectively.

The average crystallite size was calculated by diffraction line broadening using the Scherer equation $D = (0.94\lambda)/(\beta \cos \theta)$ where θ is the diffraction angle, the wavelength is represented

by λ ($\lambda = 1.542$ Å) (Cu-Kα), and β is the FWHM of the diffraction line. The estimated crystallite size for Mn_2O_3 was 12.43 nm and 11.87 nm for ZnO.

The EDX spectrum is shown in Fig. 2d demonstrating the elemental composition of as-synthesized NPs with atomic % equivalent to the bulk in good agreement with XRD analysis. Through elemental analysis, the purity and uniform composition of nanoparticles have been confirmed. EDX mapping in Fig. 3a–c depicts the uniform distribution of Zn, Mn and O in the whole area. The morphology of synthesized $ZnO-Mn_3O_4$ NPs at different magnification has been shown in Fig. 3d–f. The images present polycrystalline structures that could facilitate excellent electrochemical conductivity or catalytic diffusion of ions.[105] Moreover, the voids and spaces between such particle arrangements provide more spaces to foreign ions with enhanced electrochemical performance.[105] The TEM analysis further reveals the morphology of nanostructures at different magnification (Fig. 3g–i).

At 200 nm, nanoclusters have been observed which become clearer in Fig. 3h representing somehow porous morphology which could facilitate the efficient mass transport and electron transfer.[105] In Fig. 3i the nanostructures appear to contain some
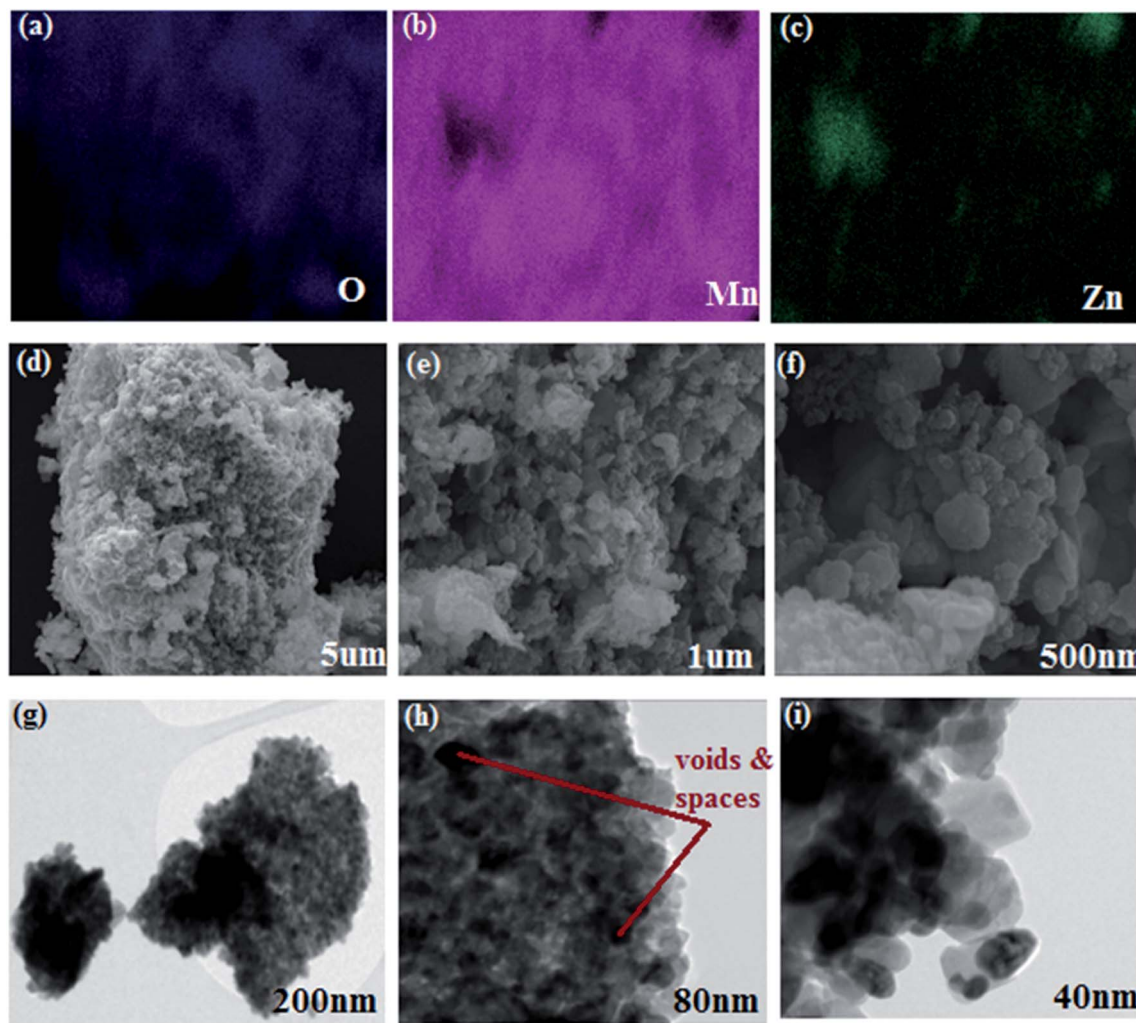
Fig. 3 (a–c) Elemental mapping images of the individual O, Zn, and Mn (d–f) SEM images (g–i) TEM images of ZnO/Mn$_3$O$_4$ NPs at different magnifications.

other nanoparticles inside indicating the formation of mixed structures of both metal oxides ZnO/Mn$_3$O$_4$. Finally, X-ray photoelectron spectroscopy (XPS) was utilized to examine the surface chemistry and oxidation states of phyto-fabricated ZnO/Mn$_3$O$_4$ NPs (Fig. 4). In the survey spectrum peaks associated with Zn, Mn, O and C can be seen (Fig. 4a). The deconvoluted spectra of Mn 2p spectrum (Fig. 4b) exhibits a doublet with peaks at binding energies of 653.59 eV and 641.78 eV corresponding to the Mn 2p$_{1/2}$ and Mn 2p$_{3/2}$ as two spin-orbital split peaks[48,101] with splitting energy of 11.81 eV. Fitting of transition metal 2p levels is difficult due to multiplet splitting as the outgoing photoelectron/core hole interacts with the d-electrons in the valence band.[107–109] This becomes even more complex for spinel compounds such as Mn$_3$O$_4$ where there is a mixture of Mn^{2+} and Mn^{3+} ions in the structure. Biesinger *et al.* have published extensive studies on multiplet splitting of transition metal core levels[109–111] based on the theoretical work of Gupta and Sen.[107,108] However no standard for Mn$_3$O$_4$ is presented in this work, so we use the approach used by Grosvenor for fitting Fe$_3$O$_4$ spectra[111] using a mixture of Mn^{2+} and Mn^{3+} multiplet

peaks (see ESI Fig. S-2(a and b)†). We find that using the expected ratio of 2 : 1 for Mn^{3+} : Mn^{2+} gives a reasonable fit compared to a 1 : 1 ratio. Fig. S-2(c) in ESI† also shows the peak fitting for MnO and it is poor, ruling out the possibility that the material is MnO. In Fig. 4b, we show the multiplet fit constrained to the values for Mn$_2$O$_3$ as suggested by Biesinger *et al.*, which gives very good agreement with the experimental data.[109] Although this may appear to be at odds with XRD and EDX data which suggest that the bulk structure is Mn$_3$O$_4$, we note that XPS is surface sensitive, and at a kinetic energy of ∼800 eV we are probing only the top 1 nm. This would be consistent with slight oxidation of the outer surface of the nanoparticles.

Fig. 4c shows the Zn 2p spectra which are fitted well with two peaks corresponding to the spin–orbit split 2p$_{3/2}$ and 2p$_{1/2}$ peaks at binding energies of 1022.2 eV and 1048.2 eV, respectively, and consistent with the presence of ZnO.[102–104]

The C 1s spectrum shown in Fig. 4d has peaks at binding energies of 284.8 eV (alkyl and aromatic C–C, C–H), 286.3 eV (C–OH, C–O–C and C–N)[52,53] and 288.7 eV (C=O).[112] C 1s peaks can be attributed to the phyto-capping molecules as well as some
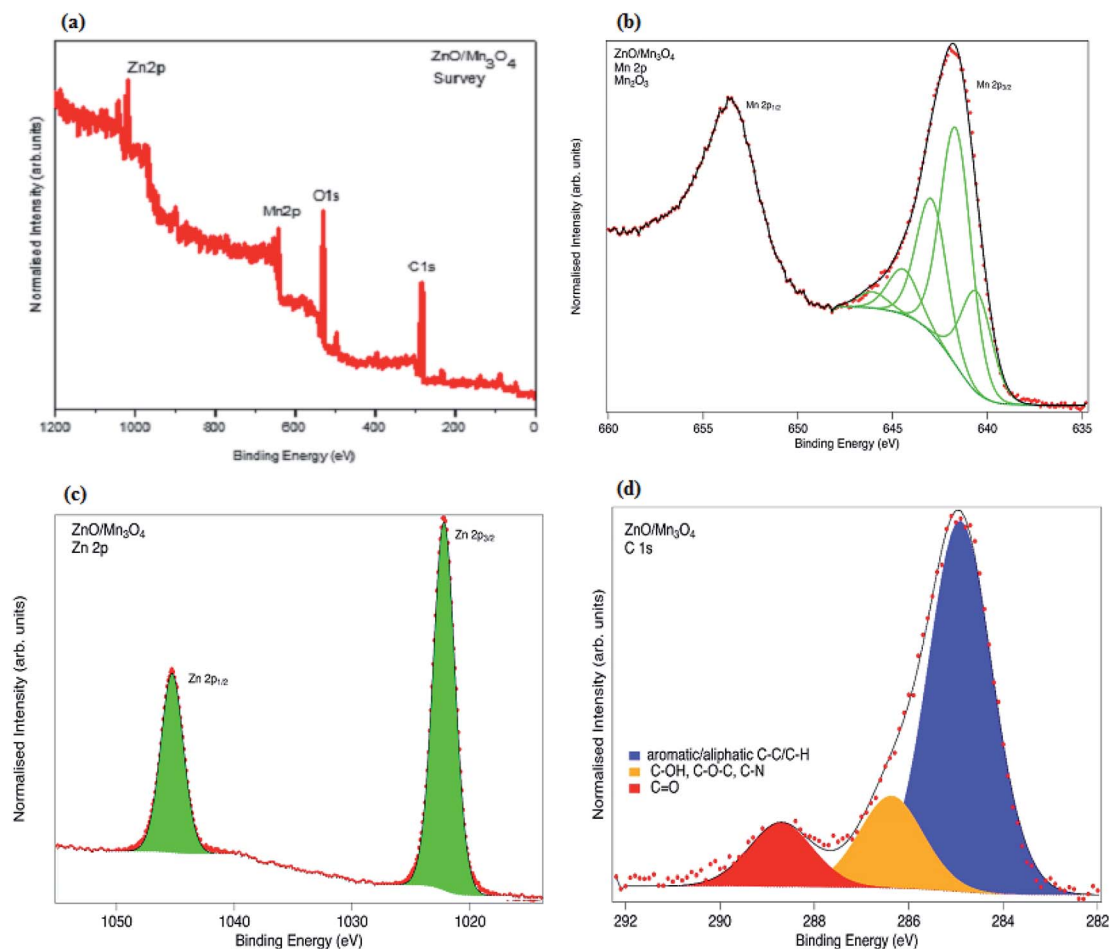
Fig. 4 XPS spectra recorded from ZnO/Mn₃O₄ NPs: (a) survey spectra, (b) Mn₂O₃, (c) Zn 2p, (d) C 1s.

contribution from adventitious carbon. In phyto-directed growth of ZnO/Mn$_3$O$_4$, residual amounts of organic material are expected because of the role of organic compounds in the synthesis and stabilization of the ZnO/Mn$_3$O$_4$ NPs. In addition it is well established that materials exposed to ambient air are covered by a layer of adventitious carbon, which will also contribute to the observed C 1s signal, particularly the C–C/C–H region at 284.8 eV.[113]

3.1. Band gap energy

UV-vis analysis of bio-synthesized NPs has been shown in Fig. 5a. Broad absorption spectra were obtained with absorbance ranging between 300 to 500 nm indicating a red shift. The band energy of the fabricated ZnO/Mn$_3$O$_4$ NPs was calculated from the absorption spectrum by using a Tauc plot as shown in Fig. 5b. The band gap is calculated using the following relation,

$$(\alpha h\nu) = B(h\nu - E_g)^{\gamma} \tag{2}$$

where α is the absorption coefficient, $h\nu$ is the incident photon energy, E_g is the optical band gap energy, B is the tailing parameter, and γ is a constant which depends on the band structure of the material. For direct gap materials it is 1/2 and

for indirect gap materials it is 2. The calculated band energy for ZnO/Mn$_3$O$_4$ NPs is 1.65 eV. The band energy value of bulk Mn$_3$O$_4$ (2.70–2.86 eV) decreases with the doping of ZnO which suggests charge transfer properties of the material with enhanced charge carriers.

3.2. Electrochemical characterization

The catalytic behavior of the ZnO/Mn$_3$O$_4$ modified Ni-foam catalyst was investigated in 1 M KOH solution at 1 mV s^{-1} sweep rate for OER and the results are shown in Fig. 6. Nickel foam (NF) was used as a mechanical support in the present investigation. Linear sweep voltammetry was performed to validate the catalytic performance of synthesized ZnO/Mn$_3$O$_4$ NPs. It was observed that the onset potential (RHE) of oxygen evolution reaction was 1.65 V and the corresponding over-potential was 0.42 V to achieve an OER current density of 10 mA cm^{-2} (Fig. 6a). The results have been compared with some reported transition metals based electrocatalysts (Table 1), the obtained over potential in present work is much lower than one of the studies reported by Chung et al., in which mesoporous Mn gave an over potential of 550 mV.[58] At the same time, benchmark catalyst RuO$_2$ has shown an over potential of 415 mV in a study by Chung et al., which is much lower than the
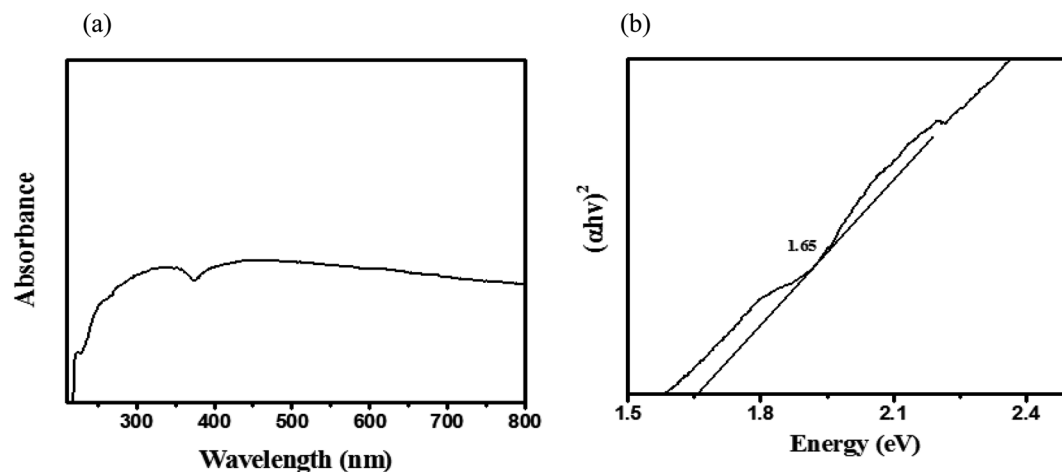
Fig. 5 (a) UV-vis absorption spectra of ZnO/Mn_3O_4, (b) band gap of ZnO/Mn_3O_4 by Tauc plot.

over potential obtained in the present investigation.[58] Commercial RuO_2 and IrO_2 are excellent OER catalyst with the low over-potential of 200 mV (in acid) and 300 mV (in alkaline) to achieve a current density of 10 mA cm^{-1} but the only drawback is that the benchmark catalyst required a special setup of proton exchange membrane electrolyzer which is very expensive and rare for large scale application in comparison with the non-precious transition metal oxide-based mixed metal oxides which are abundant and can easily be operated in alkaline medium.

The uniqueness of the present study is low-cost fabrication of non-precious mixed metal oxide nanoparticles with good electrochemical performance in a completely green and sustainable mode. Another study by Chauhan *et al.*, in which mixed metal
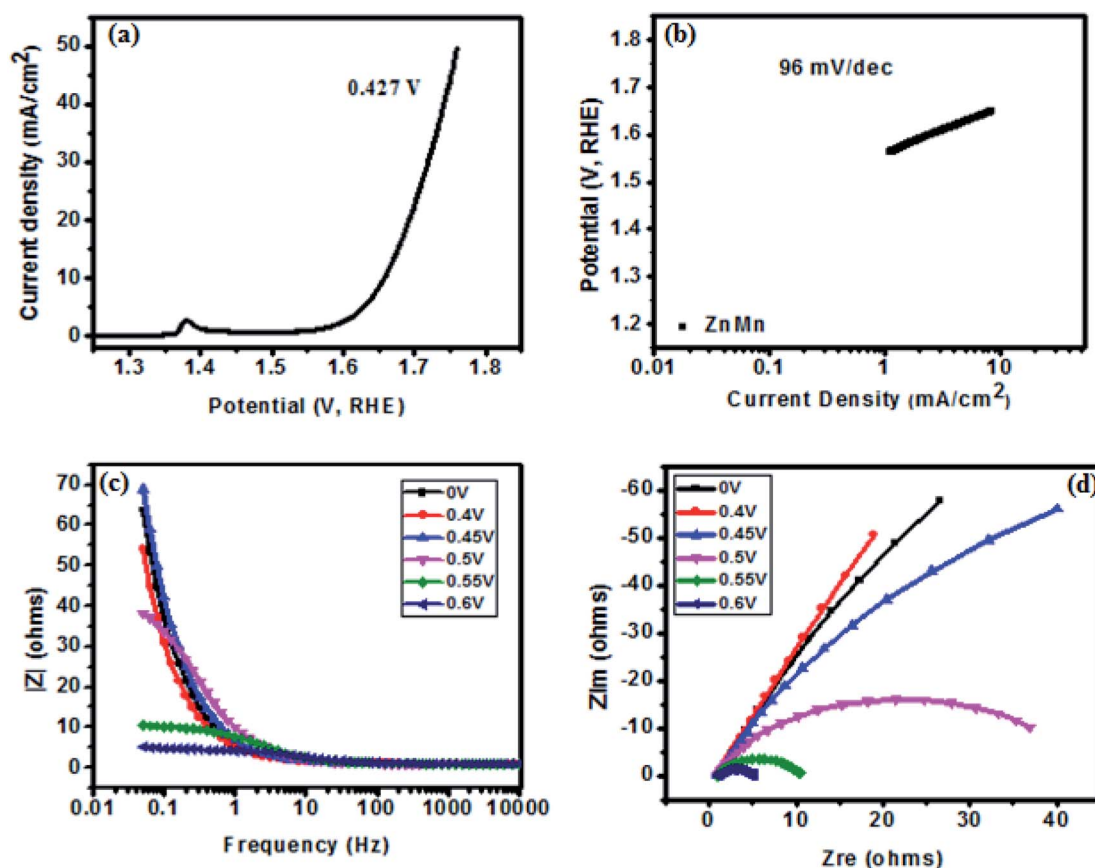

Fig. 6 OER measurements: (a) polarization curves, (b) Tafel slopes, (c) variation of impedance as a function of frequency at various over-potentials (d) Nyquist plot at various over-potentials.

Table 1 Comparison of OER performance of ZnO/Mn$_3$O$_4$ electro catalyst in comparison with transition metal/metal oxides

Catalyst	Over potential	Electrolyte	Tafel slope (mV dec^{-1})	Reference
IrO$_2$	320 mV	1 M KOH	—	64
IrO$_2$	320 mV	1 M KOH	—	65
CoMnO$_2$	390 mV	1 M KOH	95	66
Ni$_2$P nanoparticles	500 mV	1 M KOH	—	67
N-doped graphene-NiCo$_2$O$_4$ hybrid paper	434 mV	—	—	68
Co$_2$P	370 mV	1 M KOH	128	66
Co$_3$O$_4$/SWCNTS	550 mV	1 M KOH	104	69
Zn–Co–S nanosheets	390 mV	1 M KOH	136	70
Zn–Co–S nanoplates	330 mV	1 M KOH	97	70
ZnO/Mn$_3$O$_4$ NPs	420 mV	1 M KOH	96	This work

synthesized by chemical route gave very high over potential value as compared to the present study as well as demonstrated a complex synthesis approach.[59] Zhang et al. reported a polarization curve of transition metal-based NiO nanoparticles with a very high over potential of 484 mV and 486 mV for NiO@NF-4 and NiO@NF-8 to reach 10 mA cm^{-2}.[81] Furthermore, it has been reported by Lv et al. in which they demonstrated the synthesis and electrochemical performance of transition metal oxides in comparison with the state of art Pt/C electro catalyst. They proposed the synthesis approach involving the use of polyvinyl pyrrolidone (PVP), sodium thiosulfate (oxidizing agent) and exhibited an over potential of 420 mV, 422 mV and 600 mV for Co$_3$O$_4$ nano cage, NiCo$_2$O$_4$ and 20 wt% Pt/C, respectively.[82] Nevertheless, the present study revealed the environmentally friendly and cost-effective synthesis of ZnO/Mn$_3$O$_4$ low over potential of 0.42 V which outperform the transition metal/metal oxide-based particles synthesized by chemical route involving toxic chemicals and reagents as discussed earlier.

Fig. 6b shows a Tafel plot with current density on the x-axis and potential on the y-axis. The Tafel slope of the fabricated catalyst is a major indicator to demonstrate the electrochemical performance for oxygen evolution. The Tafel slope has been measured from the linear part of the curve potential (RHE) and current density which indicated good OER activity. For studying the kinetics or to reveal the prominent changes in the OER mechanism, the Tafel slope is a very important parameter,[59] since it is inversely correlated to the kinetics of the reaction i.e., smaller Tafel value correlates with faster charge transfer kinetics.[59–61] The value of Tafel slope was 96 mV dec^{-1} in this work indicating efficient kinetic behavior of the catalyst for OER. It can also be assessed from the low Tafel value that the synthesized material was well adhered on Ni-foam leading to the observed good OER performance. The Tafel value of fabricated electrode in the current study is lower than the transition non-noble metal-based binary oxides synthesized by Hu et al. in which they demonstrated Tafel value of 98 mV dec^{-1} and 125 mV dec^{-1} for benchmark RuO$_2$ and binary NiCo@NF respectively.[79] Similarly, Han et al. reported standard RuO$_2$ with a Tafel value of 128 mV dec^{-1} (ref. 80) larger than in the present study. Another study by Zheng et al. NiOH and IrO$_2$ showed a Tafel slope of 104 and 118 mV dec^{-1}.[81] In comparison with reported studies, the observed Tafel value of 96 mV dec^{-1} for OER in the present investigation is comparatively small which implies that bio-synthesized ZnO/Mn$_3$O$_4$ electro-catalyst exhibit fast reaction kinetics which results in improved OER activity.

Electrochemical impedance spectroscopy (EIS) was performed at varying potential (V vs. RHE) to estimate internal resistance (R_s) and charge transfer resistance (R_{ct}) of the fabricated electrode as shown in Fig. 6d. The cumulative resistance of electrode material, electrolyte and electrolyte/electrode interface comes under R_s.[49,50,54,56] Impedance effect can be subdivided further into high-frequency regions (HFR) and low-frequency regions (LFR). In HFR, the intercept of the semicircle on the real axis denotes R_s and the width of the semicircle graph is representative of R_{ct}.[49,50,55,56] Whereas in LFR, if the slope of impedance on the real axis is closer to Warburg angle of 45° then that exhibits low Warburg impedance and improved ion transfer or diffusion from the electrolyte to electrode showing high capacitive behavior.[51] It has been observed in present investigation that the width of semicircle is very small at voltage 0.6 V, and estimated R_s and R_{ct} values were 0.2 Ω and 5 Ω respectively. Similarly the R_{ct} value at 0.55 V was 10 Ω and increases with decreasing voltage. With decreasing voltage the semicircle becomes larger until the plot become straight at the lowest voltage. It can be assessed that in the HFR the width of the semicircle is very small, indicating the faradaic reaction driven charge transfer resistance. As the Nyquist plot is indicative of charge transfer resistance which represents a transfer of ions/charge across the electrode/electrolyte interface. It means the resistance decreased with increasing potential depicting good electrochemical transfer in terms of acceleration of charge transfer between electrolyte and electrode. The Bode plot (Fig. 6c) between impedance and frequency suggests that impedance shifts towards lower frequency with increasing voltage, exhibiting fast electron conduction of ZnO/Mn$_3$O$_4$ in good agreement with the lower value of R_{ct}.

One of the prominent aspects of present work is the incorporation of organic functional groups; methyldecylamine (C$_{11}$H$_{25}$N) comprised of C, H, N elements which affect the surface morphology of the synthesized material in term of enhancement of active sites and charge transfer properties of the electro-catalyst as depicted by the XPS analysis in which C–OH, C–O–C compounds have been identified. These results are consistent with previous studies[62,63] which demonstrates that

organic compounds *i.e.* C, H, O and N based groups are mostly derived from bioactive compounds of biomass and organic waste which enhance the catalytic performance of electrode material. Moreover, the nanostructured ZnO/Mn_3O_4 is suitable for OER as an electro catalyst due to the nano pores as explored in SEM/TEM graphs which give rise to a high surface area for efficient charge transfer in alkaline medium.

The as-synthesized electrode has also been tested for HER studies at varying potential (*V*, RHE), as shown in Fig. 7. The polarization showed an over-potential of 137 mV at −20 mA cm^{-2} at a positive potential of around 0.15. The Tafel slope of ZnO/Mn_3O_4 is very large for HER as shown in Fig. 7b. The rate of hydrogen evolution is constrained by proton adsorption on active site which cause surface poisoning and lead to deactivation of catalyst. The high value of the Tafel slope exhibits proton (H^+) adsorption on active site (Volmer step) termed as the rate-limiting step.[57,75] As in the present investigation, the HER reaction is sluggish due to the adsorption of protons on the active site. The EIS measurements towards HER have been administered and are shown in Fig. 7d as a Nyquist plot. It was observed that the semicircle increases as the voltage decreases. At a high voltage of 1.4 V, the semicircle arch is small in the high-frequency region and increases with the decrease in voltage, representing a lower resistance and better diffusion efficiency.

In HFR the width of the semicircle is very small indicating the faradaic reaction driven charge transfer resistance. This suggests the good electrochemical performance in term of charge transfer between electrodes as an electrolyte. Some fluctuation in HER result has been observed which might be because of the washing of fabricated electrode or occurrence of some intrinsic reaction due to the alkaline electrolyte. This suggests that HER results is not favorable for this catalyst. OER studies using the as-synthesized electrode material are suitable as an electro catalyst in present work. HER results can be improved by optimizing the conditions. Some of the previous literature on HER has been delineated in Table 2.

It is understood that a different catalyst behaves differently depending upon the choice of electrolyte (acidic or alkaline) as HER catalysis in acidic environment promote more efficient availability of protons as compared to the alkaline medium. The HER mechanism basically comprise three major steps for reaction mechanism which are (i) Volmer step (ii) water dissociation and (iii) formation of active hydrogen intermediates. The dissociation of ions is difficult in alkaline medium as in this case the electro-catalyst required to break the strong H–O–H bond before adsorption of H^+ on the surface followed by desorption of hydrogen from the surface.[73–75] In present work, in alkaline medium, the material is thought to leach out during dissociation so does not show any HER evolution and resulting in the curve drop down at a positive potential which is ideally
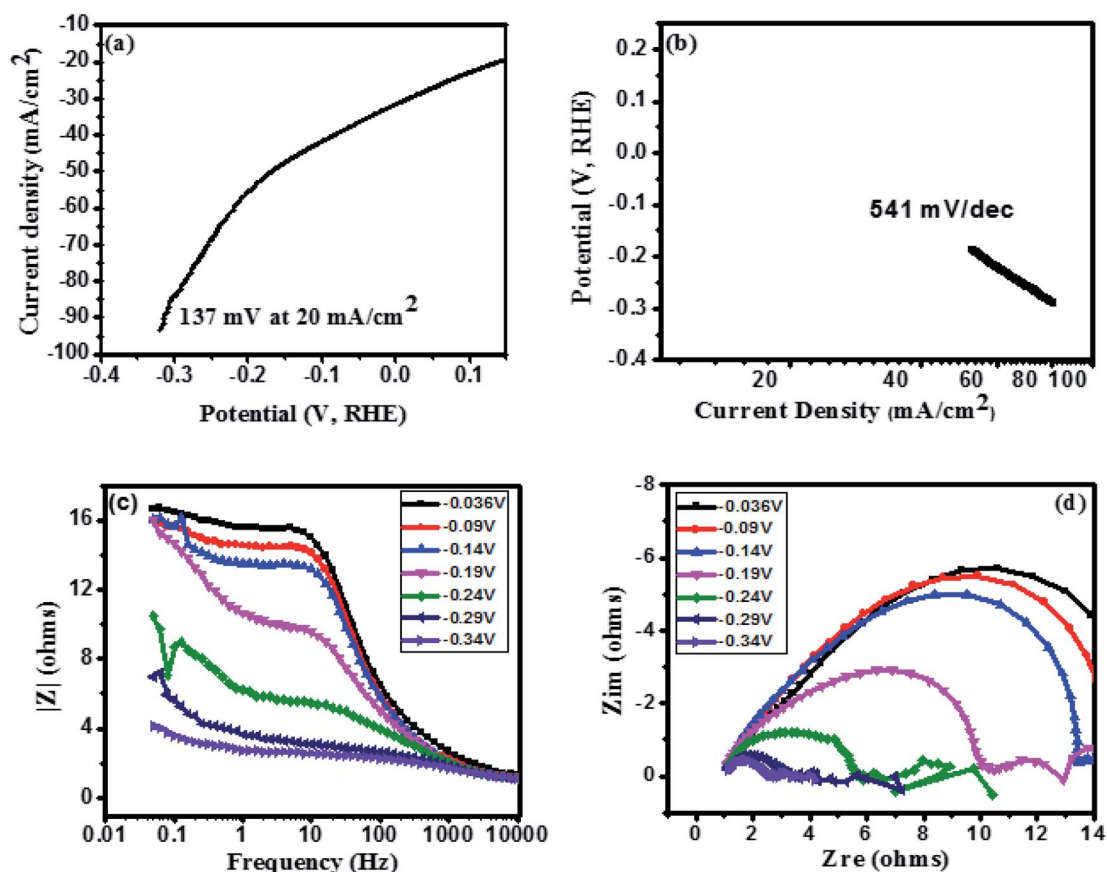

Fig. 7 HER measurements: (a) polarization curves, (b) Tafel slopes, (c) variation of impedance as a function of frequency at various over-potentials (d) Nyquist plot at various over-potentials.

Table 2 HER performance of previously studied transition metal/metal oxides

Catalyst	Over potential (mV)	Tafel slope (mV dec^{-1})	Reference
MnNi	360	—	70
Amorphous MoS_x	540	—	71
Zn–Co–S nanosheets	413	139	72
NiO@NF	494	317	73

not the property of HER mechanism. The Tafel slope in relation to kinetics of reaction mechanism again explains the mechanism since a high Tafel slope value is obtained which is not ideal for efficient HER. As discussed before it can be concluded that hydrogen adsorption and desorption are the two basic steps for successive H_2 evolution. It means that the catalyst must break the strong bond by forming a strong hydrogen bond with hydrogen atoms and weak bonding with the electrolyte to desorb hydrogen ions from the surface.[76–78] The current work suggests that the ZnO/Mn_3O_4 NPs in alkaline medium are not efficient for HER, with hydrogen adsorption as the rate-limiting step which either corrodes or over saturates the surface.

4. Conclusion

Ni-foam supported ZnO/Mn_3O_4 was fabricated by phytosynthesized greener and cost-effective route using the leaf extract of *Olea ferruginea* Royle plant completely devoid of any toxic chemicals utilization for synthetic mode. Prior to electrochemical scrutinization, the as-synthesized material was tested for structural and compositional analysis which confirmed the pure formation of ZnO/Mn_3O_4 NPs. The electrochemical performance of synthesized material was studied and found that the material could behave as a bifunctional electro-catalyst by optimizing the conditions. But on the basis of current investigation, the material is more suitable for OER performance with low over-potential and low Tafel slope indicating the fast electron transfer. Whereas, the HER results are unsatisfactory. Further, the present method is most favorable in term of commercial and environmental cost as the most greener and environmentally benign electrode material as an alternative to precious metals have been developed. The phyto-functionalized electrode material is a step towards environmental remediation and development which can be set forth in the light of present investigation.

Conflicts of interest

The authors declare no conflict of interest in this work.

Acknowledgements

References

1 H. Yang, Y. Zhang, F. Hu and Q. Wang, Urchin-like CoP nanocrystals as hydrogen evolution reaction and oxygen reduction reaction dual-electrocatalyst with superior stability, *Nano Lett.*, 2015, **15**(11), 7616–7620.

2 M. Gao, W. Sheng, Z. Zhuang, Q. Fang, S. Gu, J. Jiang and Y. Yan, Efficient water oxidation using nanostructured α-nickel-hydroxide as an electrocatalyst, *J. Am. Chem. Soc.*, 2014, **136**(19), 7077–7084.

3 L. Trotochaud, S. L. Young, J. K. Ranney and S. W. Boettcher, Nickel–iron oxyhydroxide oxygen-evolution electrocatalysts: the role of intentional and incidental iron incorporation, *J. Am. Chem. Soc.*, 2014, **136**(18), 6744–6753.

4 M. G. Walter, E. L. Warren, J. R. McKone, S. W. Boettcher, Q. Mi, E. A. Santori and N. S. Lewis, Solar water splitting cells, *Chem. Rev.*, 2010, **110**(11), 6446–6473.

5 Y. Lee, J. Suntivich, K. J. May, E. E. Perry and Y. Shao-Horn, Synthesis and activities of rutile IrO_2 and RuO_2 nanoparticles for oxygen evolution in acid and alkaline solutions, *J. Phys. Chem. Lett.*, 2012, **3**(3), 399–404.

6 M. E. Lyons and M. P. Brandon, A comparative study of the oxygen evolution reaction on oxidised nickel, cobalt and iron electrodes in base, *J. Electroanal. Chem.*, 2010, **641**(1–2), 119–130.

7 M. Gong, Y. Li, H. Wang, Y. Liang, J. Z. Wu, J. Zhou and H. Dai, An advanced Ni–Fe layered double hydroxide electrocatalyst for water oxidation, *J. Am. Chem. Soc.*, 2013, **135**(23), 8452–8455.

8 R. E. Fuentes, J. Farell and J. W. Weidner, Multimetallic electrocatalysts of Pt, Ru, and Ir supported on anatase and rutile TiO_2 for oxygen evolution in an acid environment, *Electrochem. Solid-State Lett.*, 2010, **14**(3), E5.

9 W. Hu, Y. Wang, X. Hu, Y. Zhou and S. Chen, Three-dimensional ordered macroporous IrO_2 as electrocatalyst for oxygen evolution reaction in acidic medium, *J. Mater. Chem.*, 2012, **22**(13), 6010–6016.

10 R. Li, Z. Wei and X. Gou, Nitrogen and phosphorus dual-doped graphene/carbon nanosheets as bifunctional electrocatalysts for oxygen reduction and evolution, *ACS Catal.*, 2015, **5**(7), 4133–4142.

11 X. Zhou, Y. Liu, H. Ju, B. Pan, J. Zhu, T. Ding and Q. Yang, Design and epitaxial growth of $MoSe_2$–NiSe vertical hetero nanostructures with electronic modulation for enhanced hydrogen evolution reaction, *Chem. Mater.*, 2016, **28**(6), 1838–1846.

12 G. Kwon, G. A. Ferguson, C. J. Heard, E. C. Tyo, C. Yin, J. DeBartolo and R. L. Johnston, Size-dependent sub-nanometer Pd cluster (Pd4, Pd6, and Pd17) water oxidation electrocatalysis, *ACS Nano*, 2013, **7**(7), 5808–5817.

13 N. Duraisamy, A. Numan, S. O. Fatin, K. Ramesh and S. Ramesh, Facile sonochemical synthesis of nanostructured NiO with different particle sizes and its

electrochemical properties for supercapacitor application, *J. Colloid Interface Sci.*, 2016, **471**, 136–144.

14 S. Vijayakumar, S. Nagamuthu and G. Muralidharan, Supercapacitor studies on NiO nano-flakes synthesized through a microwave route, *ACS Appl. Mater. Interfaces*, 2013, **5**(6), 2188–2196.

15 P. E. Saranya and S. Selladurai, Mesoporous 3D network Ce-doped NiO nanoflakes as high performance electrodes for supercapacitor applications, *New J. Chem.*, 2019, **43**(19), 7441–7456.

16 S. Ci, Z. Wen, Y. Qian, S. Mao, S. Cui and J. Chen, NiO-microflower formed by nanowire-weaving nanosheets with interconnected Ni-network decoration as supercapacitor electrode, *Sci. Rep.*, 2015, **5**(1), 1–12.

17 Y. Zhu, C. Cao, S. Tao, W. Chu, Z. Wu and Y. Li, Ultrathin nickel hydroxide and oxide nanosheets: synthesis, characterizations and excellent supercapacitor performances, *Sci. Rep.*, 2014, **4**, 5787.

18 S. K. Meher, P. Justin and G. Ranga Rao, Microwave-mediated synthesis for improved morphology and pseudocapacitance performance of nickel oxide, *ACS Appl. Mater. Interfaces*, 2011, **3**(6), 2063–2073.

19 J. W. Lang, L. B. Kong, W. J. Wu, Y. C. Luo and L. Kang, Facile approach to prepare loose-packed NiO nano-flakes materials for supercapacitors, *Chem. Commun.*, 2008, (35), 4213–4215.

20 M. Liu, X. Wang, D. Zhu, L. Li, H. Duan, Z. Xu and L. Gan, Encapsulation of NiO nanoparticles in mesoporous carbon nanospheres for advanced energy storage, *Chem. Eng. J.*, 2017, **308**, 240–247.

21 P. Pandurangan, T. N. Parvin, B. Soundiraraju, Y. Johnbosco, M. Ramalingam, M. Bhagavathiachari and S. S. Narayanan, Ultrasmall NiO nanoclusters modified with conical Ni(II)-SR staples for high performance supercapacitor applications, *New J. Chem.*, 2017, **41**(14), 6127–6136.

22 S. R. Gawali, D. P. Dubal, V. J. Deonikar, S. S. Patil, S. D. Patil, P. Gomez-Romero, D. R. Patil and J. Pant, Asymmetric Supercapacitor Based on Nanostructured Ce-doped NiO (Ce:NiO) as Positive and Reduced Graphene Oxide (rGO) as Negative Electrode, *ChemistrySelect*, 2016, **1**, 3471–3478.

23 X. Liu, Y. Zuo, L. Li, X. Huang and G. Li, Heterostructure NiO/Ce$_{1−x}$Ni$_x$O$_2$: synthesis and synergistic effect of simultaneous surface modification and internal doping for superior catalytic performance, *RSC Adv.*, 2014, **4**(13), 6397–6406.

24 S. Agrawal, A. Parveen and A. Azam, Microwave assisted synthesis of Co doped NiO nanoparticles and its fluorescence properties, *J. Lumin.*, 2017, **184**, 250–255.

25 T. Taşköprü, F. Bayansal, B. Şahin and M. Zor, Structural and optical properties of Co-doped NiO films prepared by SILAR method, *Philos. Mag.*, 2015, **95**(1), 32–40.

26 J. H. Zhang, G. F. Cai, D. Zhou, H. Tang, X. L. Wang, C. D. Gu and J. P. Tu, Co-doped NiO nanoflake array films with enhanced electrochromic properties, *J. Mater. Chem. C*, 2014, **2**(34), 7013–7021.

27 C. Mrabet, M. B. Amor, A. Boukhachem, M. Amlouk and T. Manoubi, Physical properties of La-doped NiO sprayed thin films for optoelectronic and sensor applications, *Ceram. Int.*, 2016, **42**(5), 5963–5978.

28 D. Chai, W. Wang, W. Dong, Y. Kang, Y. Dong and Z. Lei, Facile synthesis of a ternary Pd-PB nanoalloy: enhanced catalytic performance towards ethylene glycol electrooxidation, *Appl. Catal., A*, 2016, **525**, 1–8.

29 V. Mazumder, M. Chi, M. N. Mankin, Y. Liu, O. Metin, D. Sun and S. Sun, A facile synthesis of MPd (M = Co, Cu) nanoparticles and their catalysis for formic acid oxidation, *Nano Lett.*, 2012, **12**(2), 1102–1106.

30 A. Zalineeva, A. Serov, M. Padilla, U. Martinez, K. Artyushkova, S. Baranton, C. Coutanceau and P. Atanassov, Nano-structured Pd-Sn catalysts for alcohol electro-oxidation in alkaline medium, *Electrochem. Commun.*, 2015, **57**, 48–51.

31 Y. Liu, L. Wang, G. Wang, C. Deng, B. Wu and Y. Gao, High active carbon supported PdAu catalyst for formic acid electro-oxidation and study of the kinetics, *J. Phys. Chem. C*, 2010, **114**(49), 21417–21422.

32 K. Bhunia, S. Khilari and D. Pradhan, Monodispersed PtPdNi trimetallic nanoparticles-integrated reduced graphene oxide hybrid platform for direct alcohol fuel cell, *ACS Sustainable Chem. Eng.*, 2018, **6**(6), 7769–7778.

33 J. N. Zheng, L. L. He, F. Y. Chen, A. J. Wang, M. W. Xue and J. J. Feng, A facile general strategy for synthesis of palladium-based bimetallic alloyed nanodendrites with enhanced electrocatalytic performance for methanol and ethylene glycol oxidation, *J. Mater. Chem. A*, 2014, **2**(32), 12899–12906.

34 O. V. Kharissova, H. R. Dias, B. I. Kharisov, B. O. Pérez and V. M. J. Pérez, The greener synthesis of nanoparticles, *Trends Biotechnol.*, 2013, **31**(4), 240–248.

35 A. Siromani, K. Daniel, G. Singhal, R. Bhavesh, K. Kasaraiya, A. R. Sharma and R. P. Singh, Biosynthesis of silver nanoparticles using Ocimum sanctum (Tulsi) leaf extract and screening its antimicrobial activity, *J. Nanopart. Res.*, 2011, **13**, 2981–2988.

36 M. N. Nadagouda, G. Hoag, J. Collins and R. S. Varma, Green synthesis of Au nanostructures at room temperature using biodegradable plant surfactants, *Cryst. Growth Des.*, 2009, **9**(11), 4979–4983.

37 E. O. Dare, C. O. Oseghale, A. H. Labulo, E. T. Adesuji, E. E. Elemike, J. C. Onwuka and J. T. Bamgbose, Green synthesis and growth kinetics of nanosilver under bio-diversified plant extracts influence, *J. Nanostruct. Chem.*, 2015, **5**(1), 85–94.

38 M. Shah, D. Fawcett, S. Sharma, S. K. Tripathy and G. E. J. Poinern, Green synthesis of metallic nanoparticles *via* biological entities, *Materials*, 2015, **8**(11), 7278–7308.

39 N. J. Sushma, D. Prathyusha, G. Swathi, T. Madhavi, B. D. P. Raju, K. Mallikarjuna and H. S. Kim, Facile approach to synthesize magnesium oxide nanoparticles by using Clitoria ternatea—characterization and in vitro antioxidant studies, *Appl. Nanosci.*, 2016, **6**(3), 437–444.

40 A. Leela and M. Vivekanandan, Tapping the unexploited plant resources for the synthesis of silver nanoparticles, *Afr. J. Biotechnol.*, 2008, **7**(17), 3162–3165.

41 H. Wang, H. W. Lee, Y. Deng, Z. Lu, P. C. Hsu, Y. Liu and Y. Cui, Bifunctional non-noble metal oxide nanoparticle electrocatalysts through lithium-induced conversion for overall water splitting, *Nat. Commun.*, 2015, **6**(1), 1–8.

42 K. Geethalakshmi, T. Prabhakaran and J. Hemalatha, Dielectric studies on nano zirconium dioxide synthesized through co-precipitation process, *World Academy of Science, Engineering and Technology*, 2012, **64**, 179–182.

43 Ş. Ş. Türkyılmaz, N. Güy and M. Özacar, Photocatalytic efficiencies of Ni, Mn, Fe and Ag doped ZnO nanostructures synthesized by hydrothermal method: the synergistic/antagonistic effect between ZnO and metals, *J. Photochem. Photobiol., A*, 2017, **341**, 39–50.

44 K. S. Ahmad and S. B. Jaffri, Phytosynthetic Ag doped ZnO nanoparticles: semiconducting green remediators, *Open Chem.*, 2018, **16**(1), 556–570.

45 X. Peng, X. Bai, Z. Cui and X. Liu, Green synthesis of Pd truncated octahedrons using of firmiana simplex leaf extract and their catalytic study for electro-oxidation of methanol and reduction of p-nitrophenol, *Appl. Organomet. Chem.*, 2019, **33**(8), e5045.

46 R. S. S. Kumar, S. Murugesan, G. Kottur and D. Gyamfi Black tea: the plants, processing/manufacturing and production, *Tea in health and disease prevention*, 2013, pp. 41–57.

47 K. Vijayaraghavan, S. K. Nalini, N. U. Prakash and D. Madhankumar, One step green synthesis of silver nano/microparticles using extracts of Trachyspermum ammi and Papaver somniferum, *Colloids Surf., B*, 2012, **94**, 114–117.

48 R. P. Pohanish, *Sittig's handbook of pesticides and agricultural chemicals*, William Andrew, 2014.

49 K. Thiagarajan, J. Theerthagiri, R. A. Senthil, P. Arunachalam, J. Madhavan and M. A. Ghanem, Synthesis of $Ni_3V_2O_8$@graphene oxide nanocomposite as an efficient electrode material for supercapacitor applications, *J. Solid State Electrochem.*, 2018, **22**(2), 527–536.

50 I. S. Lee, N. Lee, J. Park, B. H. Kim, Y. W. Yi, T. Kim and T. Hyeon, Ni/NiO core/shell nanoparticles for selective binding and magnetic separation of histidine-tagged proteins, *J. Am. Chem. Soc.*, 2006, **128**(33), 10658–10659.

51 H. B. Kolodziej and B. Rozenfeld, Plasmon losses in energy spectra of electrons scattered on the surface of Fe, Co, Ni, Cu, and Zn samples, *Acta Phys. Pol., A*, 1975, **48**(6), 765–772.

52 Y. L. T. Ngo and S. H. Hur, Low-temperature NO_2 gas sensor fabricated with NiO and reduced graphene oxide hybrid structure, *Mater. Res. Bull.*, 2016, **84**, 168–176.

53 S. Maiti, A. Pramanik, T. Dhawa, M. Sreemany and S. Mahanty, Bi-metal organic framework derived nickel manganese oxide spinel for lithium-ion battery anode, *Mater. Sci. Eng., B*, 2018, **229**, 27–36.

54 S. Sahoo, S. Zhang and J. J. Shim, Porous ternary high performance supercapacitor electrode based on reduced graphene oxide, $NiMn_2O_4$, and polyaniline, *Electrochim. Acta*, 2016, **216**, 386–396.

55 C. W. Huang and H. Teng, Influence of carbon nanotube grafting on the impedance behavior of activated carbon capacitors, *J. Electrochem. Soc.*, 2008, **155**(10), A739–A744.

56 S. Khalid, C. Cao, L. Wang and Y. Zhu, Microwave assisted synthesis of porous $NiCo_2O_4$ microspheres: application as high performance asymmetric and symmetric supercapacitors with large areal capacitance, *Sci. Rep.*, 2016, **6**, 22699.

57 D. R. Cummins, U. Martinez, A. Sherehiy, R. Kappera, A. Martinez-Garcia, R. K. Schulze and M. Chhowalla, Efficient hydrogen evolution in transition metal dichalcogenides *via* a simple one-step hydrazine reaction, *Nat. Commun.*, 2016, **7**(1), 1–10.

58 C. H. Kuo, I. M. Mosa, A. S. Poyraz, S. Biswas, A. M. El-Sawy, W. Song and S. L. Suib, Robust mesoporous manganese oxide catalysts for water oxidation, *ACS Catal.*, 2015, **5**(3), 1693–1699.

59 M. Chauhan, K. P. Reddy, C. S. Gopinath and S. Deka, Copper cobalt sulfide nanosheets realizing a promising electrocatalytic oxygen evolution reaction, *ACS Catal.*, 2017, **7**(9), 5871–5879.

60 T. Shinagawa, A. T. Garcia-Esparza and K. Takanabe, Insight on Tafel slopes from a microkinetic analysis of aqueous electrocatalysis for energy conversion, *Sci. Rep.*, 2015, **5**, 13801.

61 F. Song, L. Bai, A. Moysiadou, S. Lee, C. Hu, L. Liardet and X. Hu, Transition metal oxides as electrocatalysts for the oxygen evolution reaction in alkaline solutions: an application-inspired renaissance, *J. Am. Chem. Soc.*, 2018, **140**(25), 7748–7759.

62 H. Peng, Q. Yu, S. Wang, J. Kim, A. E. Rowan, A. K. Nanjundan and J. Yu, Molecular design strategies for electrochemical behavior of aromatic carbonyl compounds in organic and aqueous electrolytes, *Adv. Sci.*, 2019, **6**(17), 1900431.

63 X. Yang, X. Liu, Y. Wang, X. Liu, Z. Kong, A. Fu and G. Song, Spray-Assisted Synthesis of MnO@C/Graphene Composites as Electrode Materials for Supercapacitors, *Energy Technol.*, 2019, **7**(6), 1800625.

64 C. C. McCrory, S. Jung, J. C. Peters and T. F. Jaramillo, Benchmarking heterogeneous electrocatalysts for the oxygen evolution reaction, *J. Am. Chem. Soc.*, 2013, **135**(45), 16977–16987.

65 J. Chang, Y. Xiao, M. Xiao, J. Ge, C. Liu and W. Xing, Surface oxidized cobalt-phosphide nanorods as an advanced oxygen evolution catalyst in alkaline solution, *ACS Catal.*, 2015, **5**(11), 6874–6878.

66 D. Li, H. Baydoun, C. N. Verani and S. L. Brock, Efficient water oxidation using CoMnP nanoparticles, *J. Am. Chem. Soc.*, 2016, **138**(12), 4006–4009.

67 A. Han, H. Chen, Z. Sun, J. Xu and P. Du, High catalytic activity for water oxidation based on nanostructured nickel phosphide precursors, *Chem. Commun.*, 2015, **51**(58), 11626–11629.

68 Y. Li, P. Hasin and Y. Wu, $Ni_xCo_{3-x}O_4$ nanowire arrays for electrocatalytic oxygen evolution, *Adv. Mater.*, 2010, **22**(17), 1926–1929.

69 J. Wu, Y. Xue, X. Yan, W. Yan, Q. Cheng and Y. Xie, Co_3O_4 nanocrystals on single-walled carbon nanotubes as a highly efficient oxygen-evolving catalyst, *Nano Res.*, 2012, **5**(8), 521–530.

70 X. Wu, X. Han, X. Ma, W. Zhang, Y. Deng, C. Zhong and W. Hu, Morphology-controllable synthesis of Zn–Co-mixed sulfide nanostructures on carbon fiber paper toward efficient rechargeable zinc–air batteries and water electrolysis, *ACS Appl. Mater. Interfaces*, 2017, **9**(14), 12574–12583.

71 B. Liu, S. Qu, Y. Kou, Z. Liu, X. Chen, Y. Wu and C. Zhong, In Situ Electrodeposition of Cobalt Sulfide Nanosheet Arrays on Carbon Cloth as a Highly Efficient Bifunctional Electrocatalyst for Oxygen Evolution and Reduction Reactions, *ACS Appl. Mater. Interfaces*, 2018, **10**(36), 30433–30440.

72 D. Merki, S. Fierro, H. Vrubel and X. Hu, Amorphous molybdenum sulfide films as catalysts for electrochemical hydrogen production in water, *Chem. Sci.*, 2011, **2**(7), 1262–1267.

73 J. Wang, F. Xu, H. Jin, Y. Chen and Y. Wang, Non-noble metal-based carbon composites in hydrogen evolution reaction: fundamentals to applications, *Adv. Mater.*, 2017, **29**(14), 1605838.

74 H. Hu, M. Qiao, Y. Pei, K. Fan, H. Li, B. Zong and X. Zhang, Kinetics of hydrogen evolution in alkali leaching of rapidly quenched Ni–Al alloy, *Appl. Catal., A*, 2003, **252**(1), 173–183.

75 N. Mahmood, Y. Yao, J. W. Zhang, L. Pan, X. Zhang and J. J. Zou, Electrocatalysts for hydrogen evolution in alkaline electrolytes: mechanisms, challenges, and prospective solutions, *Adv. Sci.*, 2018, **5**(2), 1700464.

76 R. Guidelli, R. G. Compton, J. M. Feliu, E. Gileadi, J. Lipkowski, W. Schmickler and S. Trasatti, Definition of the transfer coefficient in electrochemistry (IUPAC Recommendations 2014), *Pure Appl. Chem.*, 2014, **86**(2), 259–262.

77 J. K. Nørskov, T. Bligaard, A. Logadottir, J. R. Kitchin, J. G. Chen, S. Pandelov and U. Stimming, Trends in the exchange current for hydrogen evolution, *J. Electrochem. Soc.*, 2005, **152**(3), J23–J26.

78 J. Greeley, T. F. Jaramillo, J. Bonde, I. B. Chorkendorff and J. K. Nørskov, Computational high-throughput screening of electrocatalytic materials for hydrogen evolution, *Nat. Mater.*, 2006, **5**(11), 909–913.

79 K. Hu, M. Wu, S. Hinokuma, T. Ohto, M. Wakisaka, J. I. Fujita and Y. Ito, Boosting electrochemical water splitting *via* ternary NiMoCo hybrid nanowire arrays, *J. Mater. Chem. A*, 2019, **7**(5), 2156–2164.

80 H. Han, K. M. Kim, H. Choi, G. Ali, K. Y. Chung, Y. R. Hong and J. H. Ryu, Parallelized reaction pathway and stronger internal band bending by partial oxidation of metal sulfide–graphene composites: important factors of synergistic oxygen evolution reaction enhancement, *ACS Catal.*, 2018, **8**(5), 4091–4102.

81 J. Zheng, W. Zhou, T. Liu, S. Liu, C. Wang and L. Guo, Homologous $NiO//Ni_2P$ nanoarrays grown on nickel foams: a well matched electrode pair with high stability in overall water splitting, *Nanoscale*, 2017, **9**(13), 4409–4418.

82 X. Lv, Y. Zhu, H. Jiang, X. Yang, Y. Liu, Y. Su and C. Li, Hollow mesoporous $NiCo_2O_4$ nanocages as efficient electrocatalysts for oxygen evolution reaction, *Dalton Trans.*, 2015, **44**(9), 4148–4154.

83 S. Sharif, K. S. Ahmad, M. S. Akhtar, R. F. Mehmood, M. K. Alamgir and M. A. Malik, In situ synthesis and deposition of un-doped and doped magnesium sulfide thin films by green technique, *Optik*, 2019, **182**, 739–744.

84 S. Z. Siddiqui, M. A. Abbasi, R. T. Aziz-ur-Rehman, T. Shahzadi, M. Ajaib and K. M. Khan, Olea ferrugenia: a potential natural source of protection from oxidative stress, *J. Med. Plants Res.*, 2011, **5**(17), 4080–4086.

85 M. A. Hashmi, H. S. Shah, A. Khan, U. Farooq, J. Iqbal, V. U. Ahmad and S. Perveen, Anticancer and alkaline phosphatase inhibitory effects of compounds isolated from the leaves of Olea ferruginea Royle, *Rec. Nat. Prod.*, 2015, **9**(1), 164.

86 R. S. Zhong, Y. H. Qin, D. F. Niu, X. S. Zhang, X. G. Zhou, S. G. Sun and W. K. Yuan, Effect of carbon nanofiber surface groups on oxygen reduction reaction of supported Pt electrocatalyst, *Electrochim. Acta*, 2013, **89**, 157–162.

87 K. Artyushkova, A. Serov, S. Rojas-Carbonell and P. Atanassov, Chemistry of multitudinous active sites for oxygen reduction reaction in transition metal–nitrogen–carbon electrocatalysts, *J. Phys. Chem. C*, 2015, **119**(46), 25917–25928.

88 Z. H. Sheng, L. Shao, J. J. Chen, W. J. Bao, F. B. Wang and X. H. Xia, Catalyst-free synthesis of nitrogen-doped graphene *via* thermal annealing graphite oxide with melamine and its excellent electrocatalysis, *ACS Nano*, 2011, **5**(6), 4350–4358.

89 C. Zhang, B. Wang, X. Shen, J. Liu, X. Kong, S. S. Chuang and Z. Peng, A nitrogen-doped ordered mesoporous carbon/graphene framework as bifunctional electrocatalyst for oxygen reduction and evolution reactions, *Nano Energy*, 2016, **30**, 503–510.

90 R. Li, Z. Wei and X. Gou, Nitrogen and phosphorus dual-doped graphene/carbon nanosheets as bifunctional electrocatalysts for oxygen reduction and evolution, *ACS Catal.*, 2015, **5**(7), 4133–4142.

91 K. Qu, Y. Zheng, X. Zhang, K. Davey, S. Dai and S. Z. Qiao, Promotion of electrocatalytic hydrogen evolution reaction on nitrogen-doped carbon nanosheets with secondary heteroatoms, *ACS Nano*, 2017, **11**(7), 7293–7300.

92 T. Y. Ma, J. Ran, S. Dai, M. Jaroniec and S. Z. Qiao, Phosphorus-doped graphitic carbon nitrides grown in situ on carbon-fiber paper: flexible and reversible oxygen electrodes, *Angew. Chem., Int. Ed.*, 2015, **54**(15), 4646–4650.

93 K. Zhang, Y. Zhao, D. Fu and Y. Chen, Molybdenum carbide nanocrystal embedded N-doped carbon nanotubes as electrocatalysts for hydrogen generation, *J. Mater. Chem. A*, 2015, **3**(11), 5783–5788.

94 S. B. Jaffri and K. S. Ahmad, Biomimetic detoxifier Prunus cerasifera Ehrh. silver nanoparticles: innate green bullets for morbific pathogens and persistent pollutants, *Environ. Sci. Pollut. Res.*, 2020, 1–17.

95 I. Shaheen and K. S. Ahmad, Chromatographic identification of "green capping agents" extracted from Nasturtium officinale (Brassicaceae) leaves for the synthesis of MoO_3 nanoparticles, *J. Sep. Sci.*, 2020, **43**(3), 598–605.

96 S. P. Dubey, A. D. Dwivedi, M. Lahtinen, C. Lee, Y. N. Kwon and M. Sillanpaa, Protocol for development of various plants leaves extract in single-pot synthesis of metal nanoparticles, *Spectrochim. Acta, Part A*, 2013, **103**, 134–142.

97 T. Zahra and K. Shahzad Ahmad, Structural, optical and electrochemical studies of organo-templated wet synthesis of cubic shaped nickel oxide nanoparticles, *Optik*, 2020, 164241.

98 H. Rashid, M. A. Mansoor, B. Haider, R. Nasir, S. B. Abd Hamid and A. Abdulrahman, Synthesis and characterization of magnetite nano particles with high selectivity using in situ precipitation method, *Sep. Sci. Technol.*, 2019, 1–9.

99 C. Gervas, M. D. Khan, S. Mlowe, C. Zhang, C. Zhao, R. K. Gupta and N. Revaprasadu, Synthesis of Off-Stoichiometric CoS Nanoplates from a Molecular Precursor for Efficient H_2/O_2 Evolution and Supercapacitance, *ChemElectroChem*, 2019, **6**(9), 2560–2569.

100 M. Hou and J. Ge, Armoring enzymes by metal–organic frameworks by the coprecipitation method, in *Methods in enzymology*, Academic Press, 2017, vol. 590, pp. 59–75.

101 Z. Y. Tian, P. Mountapmbeme Kouotou, N. Bahlawane and P. H. Tchoua Ngamou, Synthesis of the catalytically active Mn_3O_4 spinel and its thermal properties, *J. Phys. Chem. C*, 2013, **117**(12), 6218–6224.

102 J. H. Zheng, Q. Jiang and J. S. Lian, Synthesis and optical properties of flower-like ZnO nanorods by thermal evaporation method, *Appl. Surf. Sci.*, 2011, **257**(11), 5083–5087.

103 J. F. Moulder, W. F. Stickle, P. E. Sobol and K. D. Bomben, in *Handbook of X-ray Photoelectron Spectroscopy*, ed. J. Chastain, Perkin-Elmer Corporation, Eden Prairie, MN, USA, 1992, p. 89.

104 J. Das, S. K. Pradhan, D. R. Sahu, D. K. Mishra, S. N. Sarangi, B. B. Nayak and B. K. Roul, Micro-Raman and XPS studies of pure ZnO ceramics, *Phys. B*, 2010, **405**(10), 2492–2497.

105 J. Jiang, J. P. Liu, X. T. Huang, Y. Y. Li, R. M. Ding, X. X. Ji and Z. H. Zhu, General synthesis of large-scale arrays of one-dimensional nanostructured Co_3O_4 directly on heterogeneous substrates, *Cryst. Growth Des.*, 2010, **10**(1), 70–75.

106 S. Shan, J. Luo, L. Yang and C. J. Zhong, Nanoalloy catalysts: structural and catalytic properties, *Catal. Sci. Technol.*, 2014, **4**(10), 3570–3588.

107 R. P. Gupta and S. K. Sen, Calculation of multiplet structure of core p-vacancy levels, *Phys. Rev. B: Solid State*, 1974, **10**(1), 71.

108 R. P. Gupta and S. K. Sen, Calculation of multiplet structure of core p-vacancy levels. II, *Phys. Rev. B: Solid State*, 1975, **12**(1), 15.

109 M. C. Biesinger, B. P. Payne, A. P. Grosvenor, L. W. Lau, A. R. Gerson and R. S. C. Smart, Resolving surface chemical states in XPS analysis of first row transition metals, oxides and hydroxides: Cr, Mn, Fe, Co and Ni, *Appl. Surf. Sci.*, 2011, **257**(7), 2717–2730.

110 A. P. Grosvenor, M. C. Biesinger, R. S. C. Smart and N. S. McIntyre, New interpretations of XPS spectra of nickel metal and oxides, *Surf. Sci.*, 2006, **600**(9), 1771–1779.

111 A. P. Grosvenor, B. A. Kobe, M. C. Biesinger and N. S. McIntyre, Investigation of multiplet splitting of Fe 2p XPS spectra and bonding in iron compounds, *Surf. Interface Anal.*, 2004, **36**(12), 1564–1574.

112 A. G. Thomas, M. J. Jackman, M. Wagstaffe, H. Radtke, K. Syres, J. Adell and N. Martsinovich, Adsorption studies of p-aminobenzoic acid on the anatase TiO_2 (101) surface, *Langmuir*, 2014, **30**(41), 12306–12314.

113 G. C. Smith, Evaluation of a simple correction for the hydrocarbon contamination layer in quantitative surface analysis by XPS, *J. Electron Spectrosc. Relat. Phenom.*, 2005, **148**(1), 21–28.